Journal of Power Sources 280 (2015) 81–89

Contents lists available at ScienceDirect

Journal of Power Sources

journal homepage: www.elsevier.com/locate/jpowsour

Metallizing porous scaffolds as an alternative fabrication method for solid oxide fuel cell anodes

Enrique Ruiz-Trejo [a, *], Alan Atkinson [b], Nigel P. Brandon [a]

[a] Department of Earth Science and Engineering, Imperial College London SW7 2AZ, United Kingdom
[b] Department of Materials, Imperial College London SW7 2AZ, United Kingdom

HIGHLIGHTS

- First report of metallic electroless-electrolytic deposits in scaffolds for anode manufacturing.
- First approach led to 1 Ωcm^{-2} area specific resistance in pure wet H_2 at 700 °C.
- Fast and low energy consumption alternative to impregnation.
- Flexibility in the fabrication of scaffold architectures is shown.

GRAPHICAL ABSTRACT

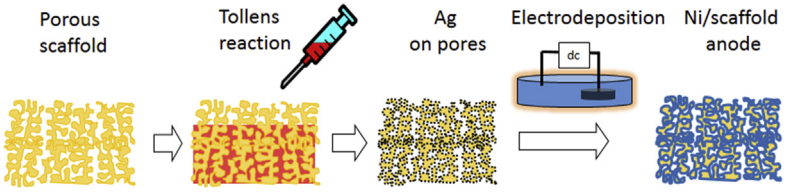

ARTICLE INFO

Article history:
Received 17 October 2014
Received in revised form
7 January 2015
Accepted 14 January 2015
Available online 17 January 2015

Keywords:
SOFC anodes
Electrodeposition
Electroless deposition
Nickel infiltration

ABSTRACT

A combination of electroless and electrolytic techniques is used to incorporate nickel into a porous $Ce_{0.9}Gd_{0.1}O_{1.90}$ scaffold. First a porous backbone was screen printed into a YSZ electrolyte using an ink that contains sacrificial pore formers. Once sintered, the scaffold was coated with silver using Tollens' reaction followed by electrodeposition of nickel in a Watts bath. At high temperatures the silver forms droplets enabling direct contact between the gadolinia-doped ceria and nickel. Using impedance spectroscopy analysis in a symmetrical cell a total area specific resistance of 1 Ωcm^2 at 700 °C in 97% H_2 with 3% H_2O was found, indicating the potential of this fabrication method for scaling up.

1. Introduction

Typically Solid Oxide Fuel Cell (SOFC) anodes are prepared by mixing thoroughly NiO and yttria stabilised zirconia (YSZ) and applying them to a substrate using ceramic forming techniques such as tape casting, spin coating or screen printing followed by co-sintering [1,2]. Using these techniques large volumes of nickel (>30 vol % and typically 50 vol %) are needed to achieve adequate electronic conductivity. Unfortunately, the resulting anodes suffer from mechanical instability upon redox and temperature cycling as nickel changes in volume, eventually damaging the mechanical stability of the cells. These fabrication methods can also limit the number of reaction sites, the so-called triple phase boundaries (TPB), achieved in the electrodes leading to reduced electrochemical performance.

A promising alternative is to fabricate first a ceramic porous scaffold using conventional or modified forming techniques [3–7] and then to deposit the metal phase by physical or chemical methods. Proceeding in this way, it is possible to control the pore size, shape and volume of the scaffold structure by adding sacrificial pore formers [8] or manufacturing scaffolds with well-defined

* Corresponding author. Department of Earth Science and Engineering, Imperial College London, Prince Consort Rd, London SW72BP, United Kingdom.
E-mail address: Enrique.ruiz-trejo@imperial.ac.uk (E. Ruiz-Trejo).

http://dx.doi.org/10.1016/j.jpowsour.2015.01.091

geometries [9]. A popular method suitable to incorporate the metal phase is infiltration, also known as impregnation, as illustrated in Fig. 1. The pores are typically infiltrated with a metallic nitrate solution and then heated to obtain the metallic oxide by decomposition. There are variations in the actual impregnating procedure – vacuum assisted, hotplate assisted, variation in solvent type and concentration, microwave-accelerated [10], etc. – but most are very similar.

It is relatively simple to obtain a small nickel particle size in the infiltrated electrodes, as the nickel phase does not experience high sintering temperatures during fabrication and a significant increase in the triple phase boundary density in the electrodes is obtained, as measured by us [11]. Infiltration enables the use of metals that cannot be processed at high temperatures, for example copper. Although, the performance of the resulting anodes is excellent and it even seems to improve H_2S tolerance [12], questions arise as to the practicability of up-scaling this procedure to make it economically feasible. Impregnation is commonly used in catalysis [13,14] where adequate loadings of metals can be achieved in a single impregnation step into a very highly porous support. In the ceramic scaffolds used in SOFC anodes the porosity is far lower, and thus only a small amount of a metal nitrate can be deposited with each impregnation, meaning that multiple impregnations are required with an energetically expensive and time-consuming calcination needed in between each. This is even more demanding when a continuous metallic pathway is required for current collection.

A simple calculation can show the limitation of the infiltration method. Let us assume that a typical screen printed ion-conducting electrolyte scaffold is 10 μm thick with an area of 1 cm^2 and a porosity of 50%. The volume occupied by the ion conductor is then 0.5 μL. Let us assume that the volume of nickel to be added is 0.1 μL or 15.18 μmol (i.e. electrolyte/Ni ratio of 83:17) leaving 40% porosity. A highly concentrated solution suitable for infiltration is 2 M, thus the total volume needed of this solution is 7.58 μL. But the available space for impregnation is only 0.5 μL on the first cycle and it decreases with subsequent infiltrations. To achieve the required volume a minimum of 19 infiltrating cycles would be needed.

In this work an alternative to the impregnation process is presented. First, the electrolyte scaffold structure is obtained by screen printing mixtures of $Ce_{0.9}Gd_{0.1}O_{2-x}$ powder (CGO) and pore formers, followed by sintering. The porous scaffold was metallized using Tollens' reaction to coat the interior surfaces with a nanometric layer of silver. This layer was then coated with nickel by electro-deposition, as illustrated in Fig. 2. This paper describes the process up to the fabrication of a symmetrical cell, which was analysed by impedance spectroscopy.

The electroless and electro-deposition of metals in anodes has been reported before but was carried out in anodes that had been manufactured by the conventional methods [15–17]. Coating with conductive carbon in a scaffold has also been reported previously [18], but the method required a high temperature (900 °C) step before electrodeposition. Electroless coating of nickel in YSZ fibres has also been reported but high temperature treatment (1300 °C) is necessary to attach Ni/YSZ fibres to YSZ excluding its use with metals such as copper [19].

2. Experimental

2.1. Scaffolds

Mixtures of commercial CGO (Fuel Cell Materials) and Poly(-methyl methacrylate) beads (⌀ = 6 μm, Microbeads AS) or glassy carbon (⌀ = 2–12 μm spherical, Sigma Aldrich) were mixed with binder (Hercules ECN-7) and dispersant (Hypermer KD15) and then suspended in terpineol [20,21]. The inks were then homogenised in a triple-roll mill. The inks were deposited by screen printing onto YSZ circular substrates (Fuel Cell Materials) of thickness approximately 175 μm and ⌀ = 2 cm. After screen printing the scaffolds were sintered at 1350 °C for 2 h in air.

2.2. Silver deposit

A layer of silver was deposited in the porous scaffolds using Tollens' reaction [22]. In a typical experiment 0.51 g of $AgNO_3$ (Sigma Aldrich) was dissolved in 30 ml solvent (2/3 water, 1/3 ethanol) and a few drops of concentrated NH_4OH were added, until a black precipitate formed and then disappeared. Next 15 ml of 0.1 M of KOH solution were added, resulting in the black precipitate reappearing. Enough NH_4OH was then added to re-dissolve all this precipitate, leaving a clear solution. The scaffolds were then added to the solution. Finally, 0.134 g of dextrose previously dissolved in 3 ml of solvent were added to the mixture and left under stirring at room temperature. The deposition of silver began after 1 min and finished within 5 min. The samples were then rinsed to eliminate the remaining reagents. The silver content was determined by the weight change before and after deposition.

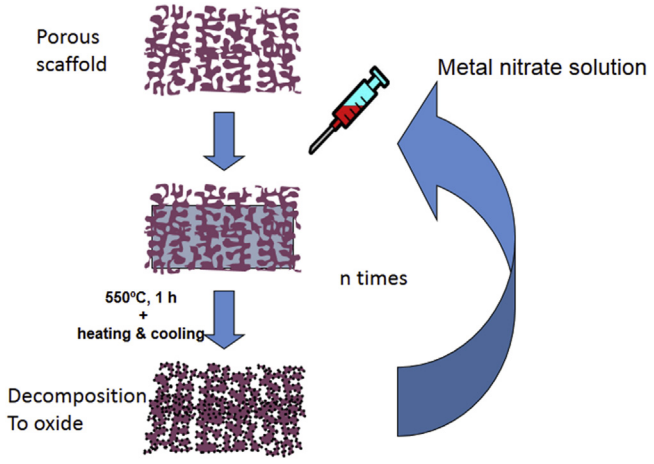

Fig. 1. Impregnation of a porous scaffold. A metal nitrate solution is infiltrated into the scaffold. This is heated to decompose the nitrate to the oxide. The operation is then repeated several times.

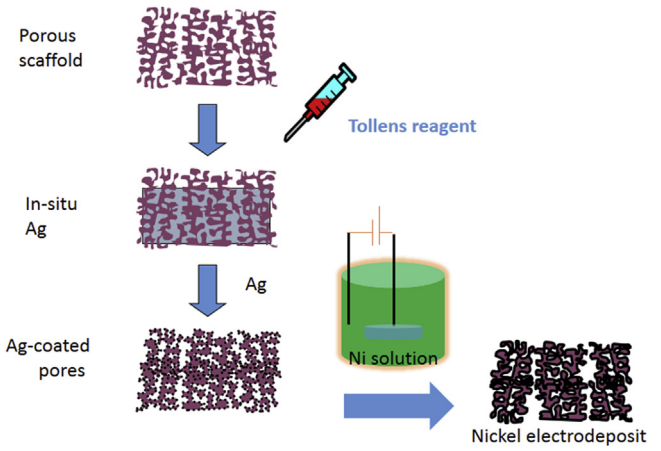

Fig. 2. Metallizing the porous network by silver using Tollens' reaction. This conductive layer is then used to electro-deposit nickel in a Watts bath.

2.3. Nickel electro-deposition

Nickel was electro-deposited from a Watts bath with $NiSO_4$, $NiCl_2$ and H_3BO_3 (Sigma Aldrich) and Surfynol (Air Products) as surfactant. Unless otherwise indicated, the electro-deposits were made at constant, but intermittent current to avoid starvation of Ni^{2+} inside the pores during deposition. Typical currents were 20 mA, with deposition times of 10 s separated by intervals of 300 s. This cycle was repeated typically 10 times. The temperature of the bath was 70 °C and held under vigorous agitation. A nickel mesh surrounded the sample to be deposited and served as the counter electrode. A silver wire shaped as a spring was connected to the silver-coated scaffold and was used as the cathode. The nickel

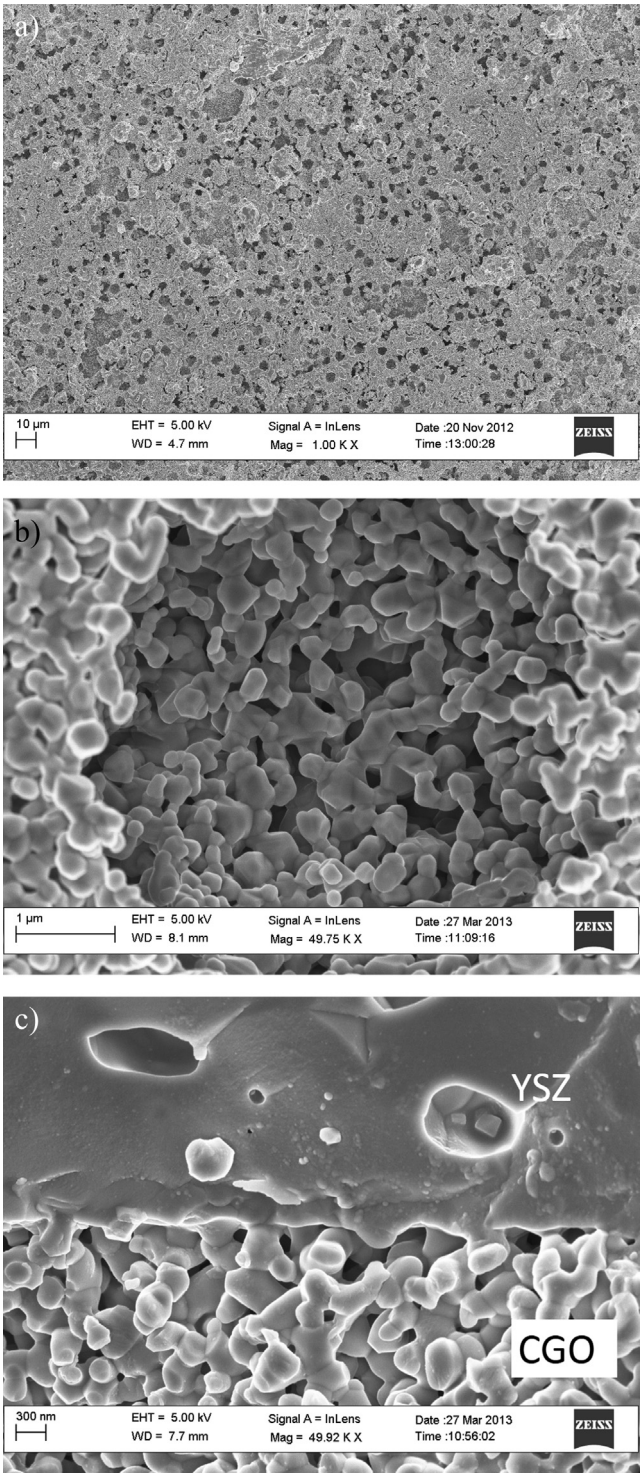

Fig. 3. Virgin porous scaffold of CGO on a YSZ dense substrate. a) Top view of the screen printed layer showing the spaces left by the sacrificial pores b) Top view of one such large pore and c) Fracture cross section showing a good adhesion with the YSZ. Porosities of the scaffolds varied between 45 and 55 vol % typically.

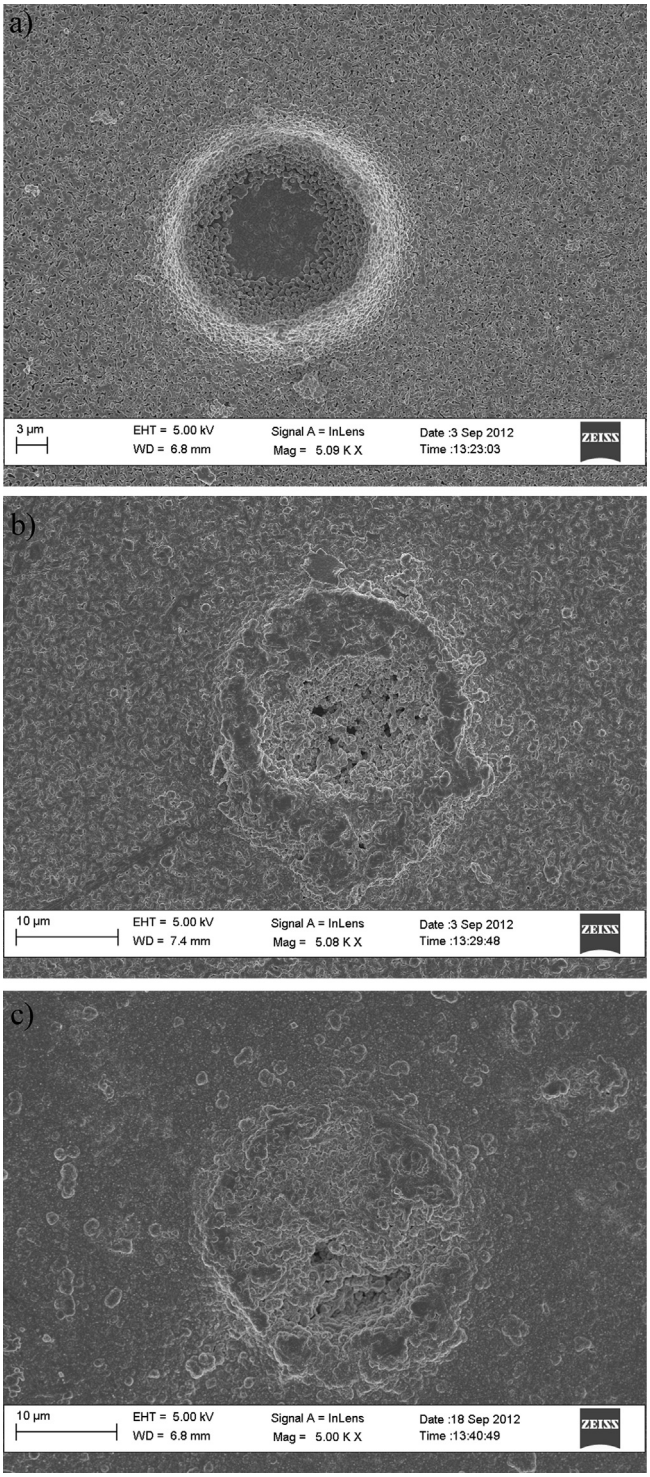

Fig. 4. a) Virgin pore in scaffold, b) after silver electroless deposition and c) after nickel electrodeposition. Images show the microstructure after metal deposition without any high temperature treatment.

content was determined by the weight change before and after deposition.

2.4. Characterisation

The structure and composition of the layers were characterised using a Field Emission Gun Scanning Electron Microscope (FEG-SEM Gemini 1525) and the phases present were identified by an X'Pert PRO MRD X-ray diffraction system.

Only one sample was used for electrochemical characterisation. The pore former used in this particular scaffold was glassy carbon. The mass of the scaffold was obtained from the weight of the YSZ substrate disc before and after deposition of the scaffold. The volume was estimated using the geometrical area of the screen printed scaffold ($\varnothing = 1$ cm) and the thickness as obtained by SEM. Impedance spectroscopy (Autolab PGSTAT302) with a Frequency Response Analyzer module was used to characterise the symmetrical cell. The impedance was measured after all the metallizing steps and then heated in 5% wet H_2 (using a room temperature water bubbler) up to 500 °C where it was left overnight before beginning the measurements. The conductivity of the plain YSZ disc (without scaffolds) was measured in air by impedance spectroscopy using Pt paint as electrodes.

The electrochemical impedance spectroscopy response was measured in the frequency range 0.1 Hz–1 MHz with a potential of 20 mV. The cell was measured between 500 °C and 750 °C in 97% $H_2 + 3\%$ H_2O. Some additional measurements with different H_2 concentrations were performed. No additional silver paint was used as current collector.

3. Results and discussion

3.1. Scaffolds

Fig. 3 shows a well-attached CGO scaffold with two types of pores: those originating from the polymeric beads close to the original size of 6 microns, and those coming from the combustion of the organic materials (binder, dispersant and organic solvent) in the 200–300 nm range. The microstructural parameters of scaffolds without large pore formers has been determined elsewhere [11]. The micro-porosity can be controlled easily by changing the size and shape of the pore former and its loading. The smaller pores provide additional surface area where the electrochemical anode reactions can take place.

3.2. Metallizing

After calcination, the scaffolds were metallized by electroless deposition of silver followed by electro-deposition of nickel. Fig. 4a shows a virgin round pore, Fig. 4b a pore with the silver coat and

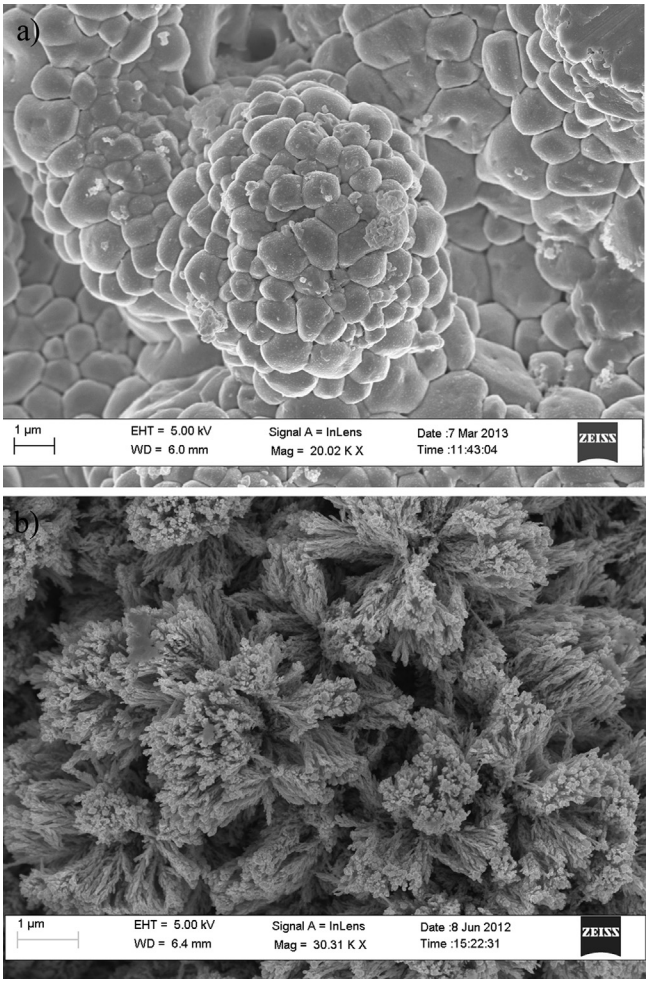

Fig. 5. a) Intermittent galvanostatic deposit of nickel and b) continuous potentiostatic deposit. The deposits were grown on a ceramic scaffold metallised by silver.

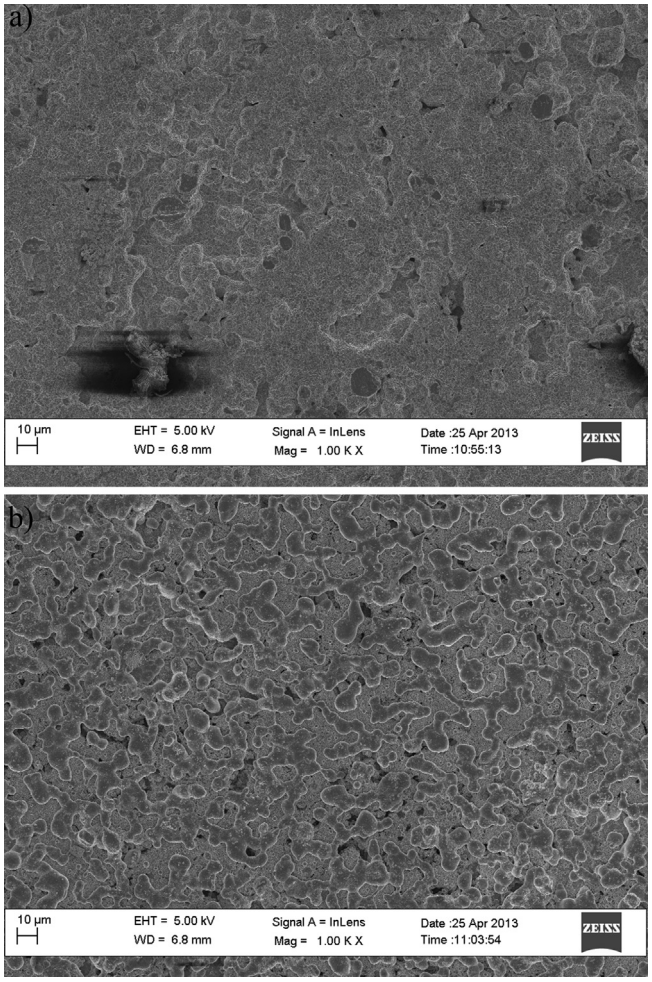

Fig. 6. a) Nickel electroplated scaffold without thermal treatment. b) Nickel electroplated scaffold after heating in a reducing environment up to 500 °C.

Fig. 4c a pore with the nickel electrodeposit. Nickel covers all the silver deposit and, as opposed to impregnation, all electrodeposited nickel is initially percolating due to the nature of the deposition technique.

These figures show that the nickel covers the surfaces of the larger pores. Nonetheless, from these images we cannot determine whether there is any nickel in the finer pores, though later we will show that nickel also penetrates into these to a certain extent.

The electro-deposition conditions have a large effect on the microstructure of the deposited nickel. One of the key parameters is the rate of nickel ion diffusion into the porous scaffold. Fig. 5a corresponds to an intermittent galvanostatic deposit at 70 °C while Fig. 5b shows a continuous deposit at 50 °C under potentiostatic conditions. The formation of dendrites in the latter indicates that the process was limited by diffusion of nickel to the surface of the cathode. These conditions might prove useful at some later stage, for example for the fabrication of a current collector, but for good penetration of the nickel into the pore structure of the scaffold, intermittent deposition appears superior. Further work on the optimisation of the electro-deposition process is underway.

3.3. Microstructural changes with temperature

The depositions of silver (ca. 100 nm thick as measured by SEM) and nickel were carried out at 25 °C and 70 °C respectively and changes in the microstructure at higher temperatures are expected due to the properties of silver, nickel and CGO. Silver and nickel do not alloy and silver does not oxidise in air, while nickel does so noticeably above 350 °C. Furthermore, silver does not wet the surface of CGO [23]. It is expected that the CGO scaffold microstructure remains relatively unchanged under operating conditions.

Fig. 6a is the original surface of the nickel electrodeposited at the top of the scaffold: the coating is uniform and all sub-micron pores of the original scaffold are temporarily blocked. Fig. 6b shows the surface of the nickel after being heated at 500 °C for 12 h in 5% wet H_2: the underlying fine porous scaffold structure is now apparent and the sub-micron pores are no longer blocked. Additionally, a network of nickel forms on the upper surface of the scaffold.

To match the performance of impregnated electrodes, a similar microstructure in the electro-deposited ones should be achieved, i.e. a large number of triple phase boundaries. Fig. 7 shows a typical microstructure for an anode formed using the multiple impregnation method (Fig. 7a) compared with one fabricated by the present process that has been oxidised at 500 °C in air (Fig. 7b). A similarity in the size and shape of the nickel oxide in both cases indicates that both methods lead to similar microstructures before reduction. Further investigation is underway.

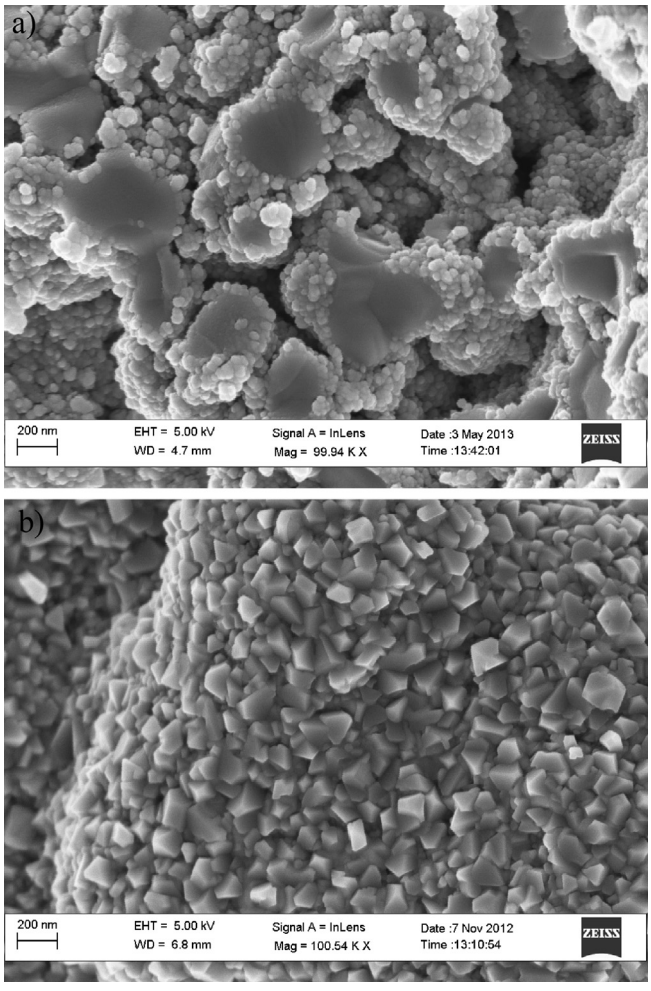

Fig. 7. a) Typical microstructure of an anode produced by impregnation compared with b) one produced by the present method after being oxidised at 600 °C in air.

3.4. Impedance characterisation of a symmetrical cell

The scaffold studied here had a thickness of 10 μm, an initial open porosity of ca 55% and was deposited on both sides of a YSZ disc. The metallizing took place in ca. 1 h and the volume percentages of the anodes was CGO 73 vol %, nickel 13 vol % and silver vol 14%. The anode had then a ratio of Ni/CGO equal to 15/85. Both sides of the disc were treated in the same way.

Fig. 8a shows the spectra obtained in 97% H_2, 3% H_2O as a function of temperature. Two semicircles were observed in most impedance spectra in the ranges of temperature and hydrogen content studied. One of the semicircles was depressed and considering the frequency interval in which it appears (10–1000 Hz), it could be associated with an electrode reaction. The second response was larger, close to semi-circular and found in the very low frequency region 0.1–10 Hz, a range usually related to diffusion effects. Fig. 8b shows the detail of the impedance spectrum at 700 °C in 97% H_2 and 3% H_2O.

The spectra were fitted to a circuit with 3 resistors (R) and 2 constant phase elements (CPE) as shown in Fig. 8b. R1 is the Ohmic resistance, R2 and CPE2 correspond to the intermediate frequency range (1000–10 Hz) while R3 and CPE3 correspond to the low frequency range (10 Hz–0.1 Hz). The intercept with the real axis is the Ohmic resistance of the cell R1 and can be compared with the expected resistance due to the YSZ alone.

Both semicircles changed with temperature but only the low frequency semicircle changed noticeably with hydrogen concentration. Fig. 8c displays the impedance plots of the sample as a function of hydrogen content at 550 °C. The low frequency values of the second semicircle suggest a diffusion process, but this signal can also be associated to a chemical capacitance. CGO can be non-stoichiometric (oxygen deficient) when reduced and this signal may be reflecting the so-called “chemical capacity”. These larger impedances had also an approximately semi-circular nature with a CPE that at times was better modelled by a capacitor. Fig. 9 shows the Ohmic resistance R1 as a function of temperature compared with that expected from the dimensions and known conductivity of the YSZ substrate [24]. The difference between the expected and the measured can be related to the contact resistances between the Pt mesh of the measuring cell and the electrodeposited Nickel, even

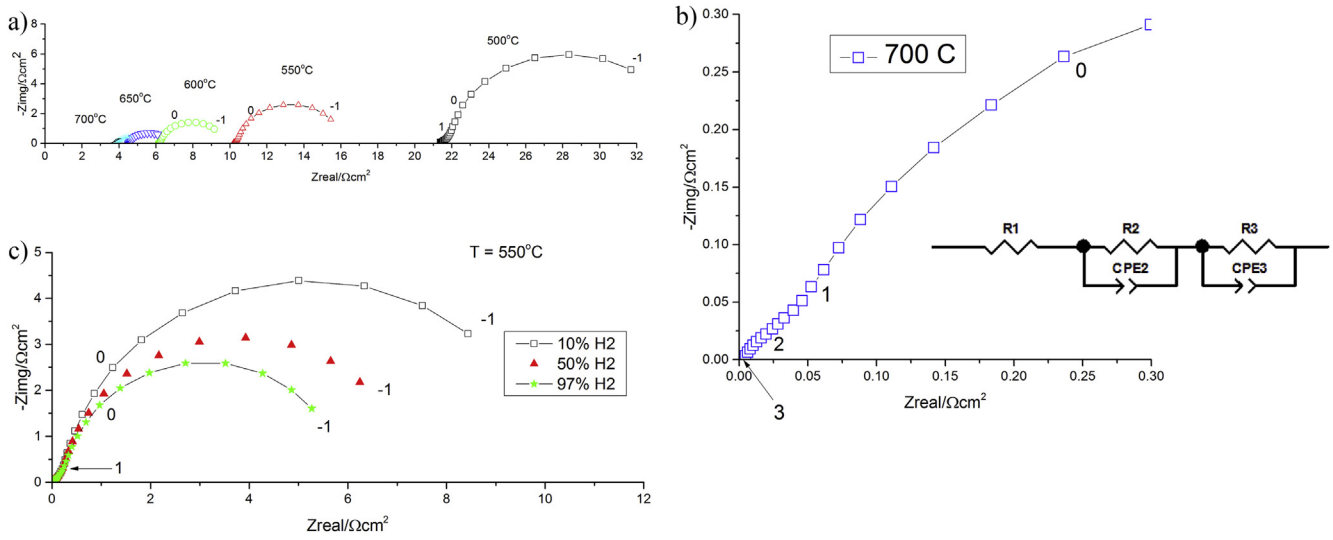

Fig. 8. a) Impedance spectra as a function of temperature for a symmetrical cell in 97% H_2 and 3% H_2O. The numbers next to the data points indicate the $\log_{10}$ of the frequency. b) Impedance spectrum for 97% H_2–3%H_2O at 700 °C. The data were fitted to the equivalent circuit shown. The Ohmic resistance R1 has been subtracted from the plot for simplicity, but it has been estimated from the fit. c) Impedance spectra as a function of partial pressure of hydrogen content at 550 °C.

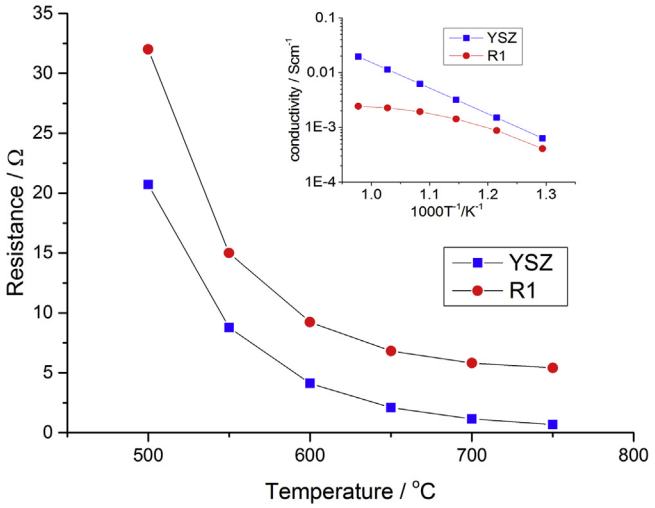

Fig. 9. Ohmic resistance for R1 and YSZ as a function of temperature. The inset shows the Arrhenius plot for the conductivity of YSZ and the conductivity associated to the element R1. The YSZ conductivity can be expressed as $\sigma T = \sigma_0 \exp(-E_a/kT)$ with $\sigma_0 = 1.89 \times 10^6$ Scm^{-1}, $E_a = 1.01$ eV and $k = 8.617 \times 10^{-5}$ eV K^{-1}.

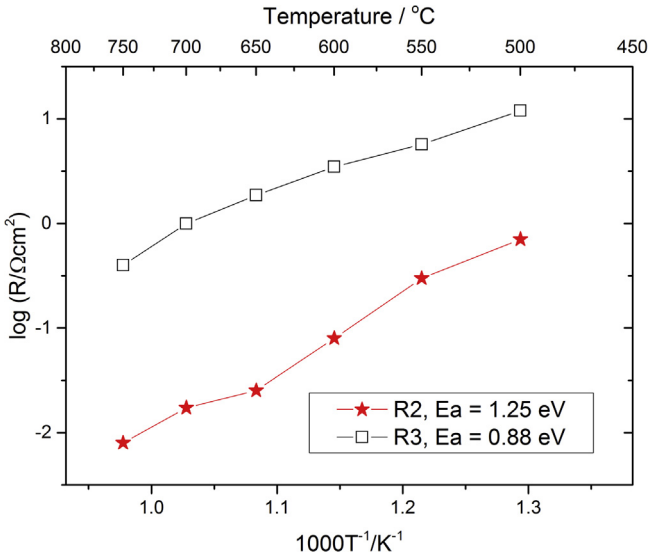

Fig. 10. Arrhenius plot of the area specific resistance for R2 (ca. 10–10,000 Hz) and R3 (ca. 0.1–10 Hz).

to the presence of a resistive layer at the interface between the CGO and the YSZ [25,26]. The inset of Fig. 9 indicates that at high temperatures the contribution from the resistance of the metal is more significant. It must be stressed that no additional silver paint was used to connect to the measuring cell and this might increase the contact resistances.

Fig. 10 displays the area specific resistance for R2 and R3. The activation energy for R2 is 1.25 eV and for R3 is 0.88 eV. The signal R2 can be compared with our previous work on similar scaffolds: a value of 0.054 Ωcm^2 for the intermediate frequency range at 50% H_2 and 690 °C [27] is not far from the value of 0.06 Ωcm^2 measured in this work. Whether R3 corresponds to the chemical capacitance of the ceria is yet to be understood but in our previous work on infiltrated scaffolds the values of resistance associated to the low frequency semicircle were considerably smaller, perhaps indicating that the homogeneity of the nickel distribution is related to this response. If this is the case, a better coverage of CGO by nickel could reduce this effect by providing reaction sites for hydrogen by increasing the number of triple phase boundaries. In fact, there is a considerably larger area of CGO that could have activity on its own.

Comparison with other data from the literature is not straightforward but it is worth collating some values to establish the potential of our technique to fabricate anodes. We shall use the total electrode polarisation (i.e. R2 + R3); in our case at 700 °C in wet H_2 we measured 1 Ωcm^2. Our recent results for a CGO scaffold with infiltrated nickel in T ~700 °C in wet H_2, show a total area specific resistance (ASR) of 0.168 Ωcm^2 using infiltration [27], where the major difference comes from the low frequency signal.

Some of the best anodes Ni/YSZ in the literature have an ASR of 0.24 Ωcm^2 at 700 °C in wet hydrogen [28] and this ASR can be considered as benchmark. Alternative anodes such as $La_{0.75}Sr_{0.25}Cr_{0.5}Mn_{0.5}O_3$ achieve 0.26 Ωcm^2 at 900 °C [29]. Ni/CGO anodes

with a meso-porous structure exhibit 0.26 Ωcm^2 at 675 °C [30], nanocrystalline thin films reach an extrapolated value of 0.18 Ωcm^2 at 700 °C [31] and finally for spin-coated samples 2.5 Ωcm^2 is reported [31]. It is clear that for the non-optimised manufacturing process presented in this work the value of 1 Ωcm^2 is very promising.

Fig. 11 shows an SEM image of the electrode after the impedance spectroscopy test. That nickel can penetrate into the larger pores has been shown clearly in Fig. 4c, while Fig. 11 shows that nickel can penetrate into the finer sub-micron porous structure, but to a lesser degree. It can also be seen that there is good contact between Ni and the CGO scaffold.

Fig. 12a shows the top layer of the scaffold. EDX spectra 2 and 3 show that some nickel and silver has de-wetted the CGO surface, forming a network over the top of the scaffold. Although the network blocks the pores exactly underneath, the total surface of the pores is considerable larger than that occupied by the metal network and should not block the diffusion of gases. See a quantification of the microstructural parameters in Ref. [11]. Silver and nickel are immiscible and silver does not wet CGO, so it is therefore not surprising to see them separate. This sample was heated in reducing atmospheres where the metallic phase had a chance to reorganise leading to the silver separation and de-wetting. Spectrum 1 shows that there is nickel inside the finer pore network but the EDX does not reveal the presence of any silver. This contact is of critical importance as its presence is required to maximise the triple phase boundary density.

Fig. 12b is a cross section showing the presence of silver throughout the electrode. Nickel can mainly be seen close to the outer surface (spectrum 3), but is also present deeper into the electrode (spectra 1 and 2).

3.5. Final remarks

Here, we will finally return to a point mentioned in the introduction to emphasize the potential of the electro-deposition technique. To be scalable the manufacturing of anodes must be fast and performed at low temperatures if possible in order to produce a fine microstructure with a high density of TPB reaction sites. The energy consumption for the electrodeposit used was minimal, with currents of 20 mA and voltages <1 V, the power consumed was ca. 20 mW during deposits; keeping the solution at 70 °C consumed more energy. Impregnation is slow as the process has to be repeated many times to achieve percolation, with a heat-treatment after each impregnation. The concentration of the impregnating solution can be increased, but there is a limit to the solubility of the nitrate and an increase in the viscosity reduces the chance of a good penetration into the pore network. Finally, the decomposition itself of nitrate to oxide requires heating the entire scaffold to at least 500 °C. A typical furnace has a power consumption of kW considerably larger than the 20 mW used in the deposit. Although in principle one could introduce the infiltrated samples into a furnace that is already at this temperature to decompose the nitrate, this can be detrimental to the mechanical stability of the scaffold, the electrolyte or other parts of the cell due to the thermal shock. Every single cycle of impregnation as shown in Fig. 1 takes at least 1 h as currently carried out and there is the additional drawback of the energy involved in each step. The complete process for fabricating the anode by repeated impregnation requires typically 19 h. On the other hand, the electrodeposition process takes, for similar content of nickel, around 1 h avoiding repetitive thermal treatments. As described here, the silver deposit is far from being optimised and scaling up will require optimisation of the unit operations. Immediate improvement can be obtained by using smaller amounts, coat several scaffolds at the same time or use a micropipette to infiltrate the Tollens reagent directly into the scaffold.

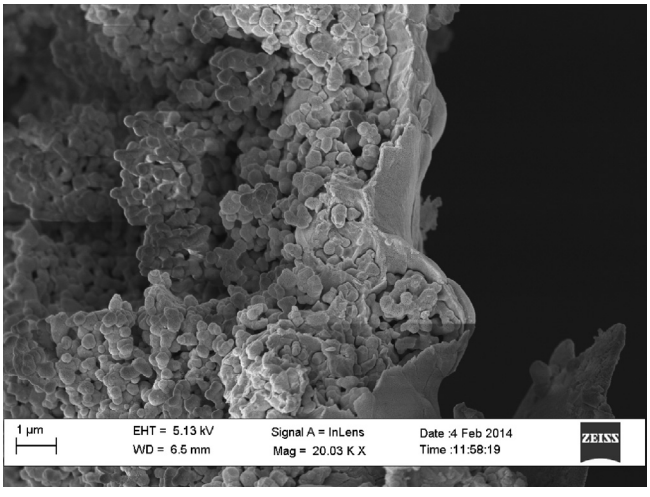

Fig. 11. Cross section with Nickel incorporated by electrodeposition and after high temperature measurements in wet hydrogen.

4. Conclusions

Porous CGO scaffolds were fabricated by screen printing ceramic powder and pore-former mixtures onto YSZ discs followed by sintering. Two types of pores were observed in the backbone, the first type are relatively large (a few microns) originated from burning out the pore formers. The loading of these pore formers in the ink can be varied and therefore a larger porosity can be achieved if desired. The second type of porosity is a network of finer pores, with diameters in the range 200–300 nm, that probably resulted from the evaporation of the organic additives used in the slurry ink. They are less easily controlled, but are important because they provide a large potential reaction surface.

Silver was first deposited onto the internal pore walls of the scaffolds by electro-less plating and then nickel was electro-deposited on top of the silver. This approach to fabricating anodes is reported here for the first time in the literature. The relatively large pores created by the pore-formers were easily coated with silver and then with nickel. The finer sub-micron pore structure could also be penetrated by the nickel as shown by SEM, but its extent and coverage still needs optimisation.

The low temperature nickel and silver microstructure changes dramatically as temperature is increased. First, silver agglomerates on the surface of CGO; leading to the desired contact of nickel with CGO and the generation of triple phase boundaries. The nickel metal also agglomerated when heated in 5% wet hydrogen. In particular, at the surface of the scaffold a percolating network of nickel was found.

Initial electrochemical impedance studies of a symmetrical cell fabricated using this process showed two semicircles in the Nyquist plot: one at intermediate frequency and one at low frequency. The intermediate frequency response R2 had a very small polarisation resistance 0.06 Ωcm^2 at 600 °C in 97% H_2 + 3% H_2O and is comparable to our previous work using standard impregnation methods. The low frequency process had a polarisation resistance that was one order of magnitude greater than the intermediate frequency process. At the present time the mechanism of the low frequency process is not understood but it might be related to the uneven distribution of nickel in the scaffold.

The total area specific resistance at 700 °C was 1 Ωcm^2 and given

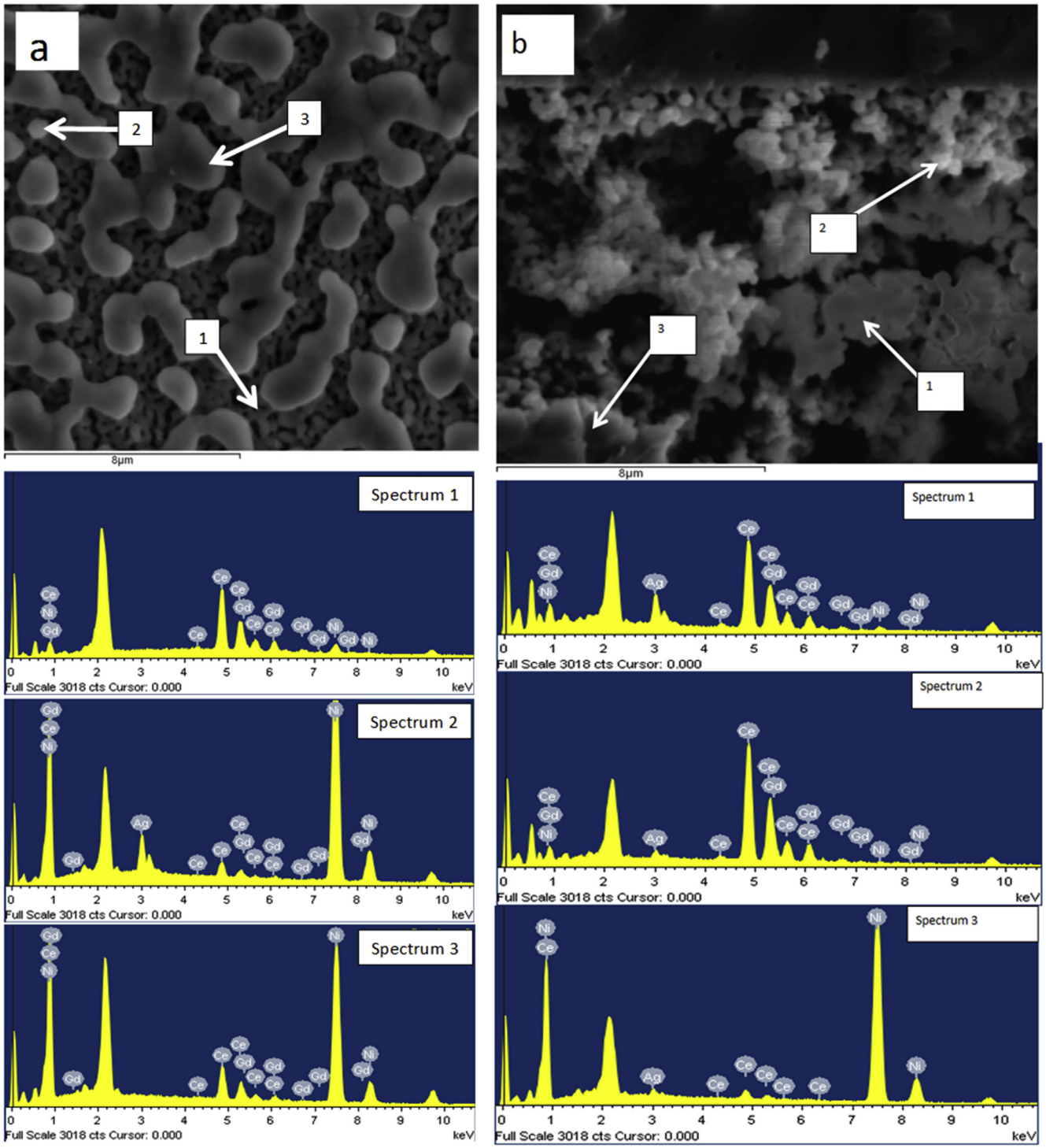

Fig. 12. EDX analysis on a sample after test in symmetrical mode a) Top layer of the Ni/Ag/CGO scaffold showing some dewetting and b) Cross section showing some nickel and silver in the porous structure. Gold at 2.2 eV is not labelled.

that this is the first report on the electroless and electrolytic metallizing approach to anode manufacturing in a scaffold, it is an encouraging result. Hence in summary, although the distribution of nickel needs to be further improved, the results indicate that this fabrication process is a promising technique that can be scaled for large volume manufacture.

Acknowledgements

ERT would like to thank funding provided by the EPSRC Advancing Biogas Utilization through Fuel Flexible SOFC project (No EP/I037016/1). We thank Dr. P. Boldrin for sample in Fig. 7a and Dr V. Duboviks for the conductivity measurements of the YSZ substrates.

References

[1] N.Q. Minh, J. Am. Ceram. Soc. 76 (1993) 563–588.
[2] S. Gamble, Mater. Sci. Tech-Lond. 27 (2011) 1485–1497.
[3] S.P. Jiang, Mater. Sci. Eng. A 418 (2006) 199–210.
[4] A.N. Busawon, D. Sarantaridis, A. Atkinson, Electrochem. Solid State Lett. 11 (2008) B186–B189.
[5] G. Kim, G. Corre, J.T.S. Irvine, J.M. Vohs, R.J. Gorte, Electrochem. Solid State Lett. 11 (2008) B16–B19.
[6] L.J. Gauckler, U.T. Gonzenbach, A.R. Studart, E. Tervoort, I. Akartuna, Cfi-Ceramic Forum Int. 84 (2007). E36–E36.
[7] E. Ruiz-Trejo, J.T.S. Irvine, Solid State Ion. 252 (2013) 157–164.
[8] A. Atkinson, S. Barnett, R.J. Gorte, J.T. Irvine, A.J. McEvoy, M. Mogensen, S.C. Singhal, J. Vohs, Nat. Mater. 3 (2004) 17–27.
[9] J.C. Ruiz-Morales, D. Marrero-Lopez, J. Canales-Vazquez, P. Nunez, J.M. Dominguez-Gonzalez, Fuel Cells 11 (2011) 144–149.
[10] E. Ruiz-Trejo, A.K. Azad, J.T. Irvine, J. Electrochem. Soc. 162 (2015) F273–F279.
[11] M. Kishimoto, M. Lomberg, E. Ruiz-Trejo, N.P. Brandon, J. Power Sources 266 (2014) 291–295.
[12] B. Mirfakhraei, S. Paulson, V. Thangadurai, V. Birss, J. Power Sources 243 (2013) 95–101.
[13] A. Vandillen, R. Terorde, D. Lensveld, J. Geus, K. Debjong, J. Catal. 216 (2003) 257–264.
[14] A. Trovarelli, Catal. Rev. Sci. Eng. 38 (1996) 439–520.
[15] E.W. Park, H. Moon, M.-s. Park, S.H. Hyun, Int. J. Hydrog. Energy 34 (2009) 5537–5545.
[16] S. Jung, M.D. Gross, R.J. Gorte, J.M. Vohs, J. Electrochem. Soc. 153 (2006) A1539–A1543.
[17] A. Rismanchian, J. Mirzababaei, S.S.C. Chuang, Catal Today. doi:10.1016/j.cattod.2014.05.012.
[18] S.W. Jung, J.M. Vohs, R.J. Gorte, J. Electrochem. Soc. 154 (2007) B1270–B1275.
[19] L. Li, P. Zhang, R. Liu, S.M. Guo, J. Power Sources 196 (2011) 1242–1247.
[20] M.R. Somalu, N.P. Brandon, J. Am. Ceram. Soc. 95 (2012) 1220–1228.
[21] M.R. Somalu, V. Yufit, D. Cumming, E. Lorente, N.P. Brandon, Int. J. Hydrog. Energy 36 (2011) 5557–5566.
[22] B. Tollens, Ber. Dtsch. Chem. Ges. 15 (1882) 1635–1639.
[23] P. Seeharaj, A. Atkinson, Solid State Ion. 204 (2011) 46–52.
[24] J. Vanherle, A.J. Mcevoy, K.R. Thampi, J. Mater. Sci. 29 (1994) 3691–3701.
[25] K. Eguchi, N. Akasaka, H. Mitsuyasu, Y. Nonaka, Solid State Ion. 135 (2000) 589–594.
[26] A. Tsoga, A. Gupta, A. Naoumidis, P. Nikolopoulos, Acta. Mater. 48 (2000) 4709–4714.
[27] M. Lomberg, E. Ruiz-Trejo, G. Offer, N.P. Brandon, J. Electrochem. Soc. 161 (2014) F899–F905.
[28] R. Barfod, A. Hagen, S. Ramousse, P.V. Hendriksen, M. Mogensen, Fuel Cells 6 (2006) 141–145.
[29] S. Tao, J.T.S. Irvine, Nat. Mater. 2 (2003) 320–323.
[30] L. Almar, B. Colldeforns, L. Yedra, S. Estrade, F. Peiro, A. Morata, T. Andreua, A. Tarancon, J. Mater. Chem. A 1 (2013) 4531–4538.
[31] M. Chen, B.H. Kim, Q. Xu, B.G. Ahn, D.P. Huang, Solid State Ion. 181 (2010) 1119–1124.